Biophysical Journal, Volume *115*

Supplemental Information

Insights into the Cooperative Nature of ATP Hydrolysis in Actin Filaments

Harshwardhan H. Katkar, Aram Davtyan, Aleksander E.P. Durumeric, Glen M. Hocky, Anthony C. Schramm, Enrique M. De La Cruz, and Gregory A. Voth

Supporting Material

Insights into the cooperative nature of ATP hydrolysis in actin filaments

Harshwardhan H. Katkar,[1] Aram Davtyan,[1] Aleksander E. P. Durumeric,[1] Glen M. Hocky,[1] Anthony C. Schramm,[2] Enrique M. De La Cruz,[2] Gregory A. Voth[1,*]

Affiliations:

[1]Department of Chemistry, Institute for Biophysical Dynamics, and James Franck Institute, University of Chicago, Chicago, IL, USA.

[2]Department of Molecular Biophysics and Biochemistry, Yale University, New Haven, CT, USA.

UCG MODEL

The UCG model was parameterized using three all-atom actin filament simulation trajectories corresponding to the three states of the bound nucleotide. Details of the all-atom simulations are provided below.

All-atom simulations

All-atom simulations of periodic actin filaments were performed in Gromacs (version 5.1.4)(1), using a protocol similar to Ref. (2). Briefly, a single actin subunit based on the Oda structure (Protein Data Bank structure 2ZWH) (3), consisting of a particular state of the bound nucleotide (either ATP, ADP-P_i or ADP, the former two were obtained by replacing the nucleotide ADP in the Oda structure with existing equilibrated simulations of ATP and ADP-P$_i$ bound actin, with positions of replaced nucleotides found by aligning positions of actin subunits between the two (4)) was repeated along with a shift of 27.59 Å and a rotation of 166.6°, such that 13 repetitions of the subunit formed a single semi-periodic repeat of the actin helical structure. The simulation box was chosen such that the filament interacted with its own image in the periodic z-direction, mimicking a virtually infinite length filament. The system was solvated with TIP3P water and neutralized using salt ions, both of these tasks performed using VMD (5). The energy of the system was minimized, followed by gradual heating to increase the temperature from 0 K to 310 K, using the molecular dynamics code NAMD (6). The system was equilibrated at a temperature of 310 K and a pressure of 1 atm, until the root-mean-square deviation of the entire filament from its initial configuration reached a plateau. Production runs were performed using the terminal state of the system during equilibration, using the v-rescale thermostat (7) and the Parrinello-Rahman barostat implemented in Gromacs. The CHARMM27+CMAP force-field was used in these simulations (8).

Three AA simulation trajectories were obtained, one for a pure ATP bound actin filament, one for a pure ADP-P$_i$ bound actin filament, and one for a pure ADP bound actin filament. Each of these AA trajectories was used to obtain CG models for the filaments with corresponding states of the bound nucleotide.

Pair-wise interactions

The pair-wise interactions between CG beads were divided into two categories, the intra-subunit interactions and the inter-subunit interactions. The intra-subunit interactions, between CG bead i and j at a distance r_{ij} belonging to the same actin subunit, were modeled using the harmonic potential U_b, as

$$U_b(r_{ij}) = k(r_{ij} - b)^2. \tag{1}$$

Here, k and b are the bond stiffness and zero energy bond length respectively. The inter-subunit interactions, between CG beads belonging to two different actin subunits, were modeled using inverted Gaussian interaction potential U_G, as

$$U_G(r_{ij}) = \frac{H}{\sigma_h\sqrt{2\pi}} \exp\left[-\frac{(r_{ij} - r_{mh})^2}{2\sigma_h^2}\right], \tag{2}$$

where parameters H and σ_h govern the depth and width, and are related to the bond stiffness in the harmonic potential, while r_{mh} governs the position of the minimum of the potential and is related to the equilibrium bond length in the harmonic potential.

Interaction parameters between a pair of CG particles with the same nucleotide state were obtained by constructing a hetero-elastic network model (hENM) based on the underlying all-atom simulations of pure state filaments. The parameters k and b for all pairs of intra-subunit CG beads were obtained from the hetero-elastic network model. The parameters H, σ_h and r_{mh} for all pairs of inter-subunit CG beads were obtained by least-square fitting of the corresponding harmonic potential U_b, obtained from the hENM, to the inverted Gaussian interaction potential U_G in the

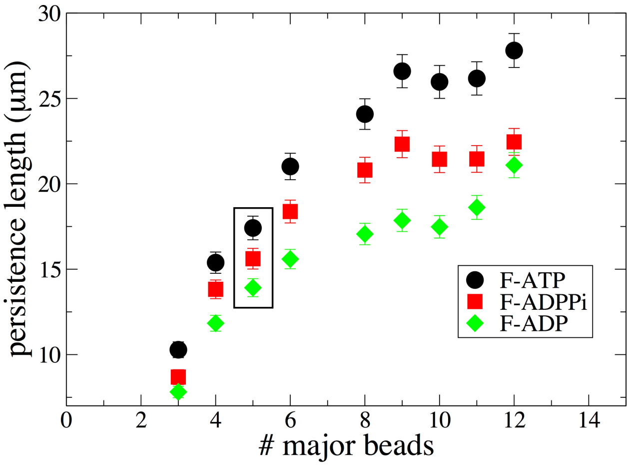

Figure S1: Persistence length of ATP, ADP-P_i and ADP bound actin filaments, as a function of the number of major beads. The major beads are chosen in the order of increasing CG indices.

region where $U_b \leq 3$ kcal/mol. The inter-subunit beads interacted with springs only between a subset of CG sites that we call *major beads* and these inter-subunit springs were restricted to bead pairs that are up to two actin subunits apart in the filament.

Figure S1 shows the variation in persistence length for the three states of bound nucleotide, obtained from the coarse-grained model simulated in LAMMPS MD software (9) using Langevin dynamics. Each data-point was calculated as an average over five simulation runs, with each initiated using a different seed for random force and initial velocity generation. For a given state of bound nucleotide, the filament became more flexible as the number of major beads decreased.

Since the persistence length with 5 major beads (corresponding to CG bead indices 1 to 5 in Figure 1 of main text) agreed best with known persistence lengths in the literature, 5 major beads were used in the rest of the manuscript. Given the difficulty in accurately measuring persistence length in experiments and the wide range of experimental values reported in literature that varies with solution conditions, we picked a value that is consistent with the reported range (10-18). The 5 major beads in an actin subunit roughly correspond to the four major sub-domains in actin and the D-loop region (see Figure 1 of main text). The D-loop region inserts into actin's barbed end "target binding cleft" and is an important mediator of longitudinal interactions in the filament (4, 13, 19-23). This provided additional motivation for including at least these 5 major beads in our model. Note that the dependence of persistence length on the number of major beads seen from Figure S1 was specific to the choice of restricting inter-subunit springs to be between subunits that were up to two subunits apart in the filament. Further, based on our previous work (14), the persistence length was expected to increase with the number of major beads as equivalent CG bead pairs had identical springs between them in our model. Thus, each subunit of a given nucleotide state experienced the same force-field. Although including heterogeneity in the force-field similar to Ref. (14) would result into a more stable persistence length across different major beads, it would increase complexity of the resulting model since conformational behavior of each subunit would be different in a heterogeneous filament.

Pair-wise interactions for the mixed state

The nucleotide discrete state dynamics of actin subunits in the filament is allowed by the UCG model. Thus, during a particular simulation run, a given subunit can change its state from ATP to ADP-P$_\mathrm{i}$ and from ADP-P$_\mathrm{i}$ to ADP. This leads to the possibility of frequently observing several different combinations of the nucleotide states for neighboring subunits in a filament.

In our model, the pair-wise interactions were limited to be between subunits that are up to two neighbors apart along the filament. The pair-wise interactions between CG beads of neighboring subunits in the same state, say both ATP, were obtained by constructing a hENM using all-atom simulations of the ATP bound actin filament (pure state), and converting to Gaussian potentials. Similarly, pair-wise interactions between CG beads, both belonging to ADP-P$_\mathrm{i}$ (or ADP) bound subunits were obtained from all-atom simulations of ADP-P$_\mathrm{i}$ (or ADP) bound actin filaments, respectively. However, when the two CG beads belong to subunits bound to dissimilar nucleotides, the pair-wise interactions were not obtained directly from all-atom simulations via direct hENM parametrization. Generally, hENM parametrization captures fluctuations in the positions of CG beads; however, the nearby neighbors of a mixed nucleotide state filament likely influence such fluctuations. A suitable parametrization assuming a reasonable number of spring types would average over all such possible nucleotide state combinations of neighbors. However, exhaustively performing all-atom simulations of different combinations of nucleotide states in the filament is computationally prohibitive. Given that each CG bead belonging to a subunit can interact with another CG bead belonging to one of five consecutive subunits (including other CG beads within the same subunit), there are 3^5=243 possible combinations of nucleotide states between five consecutive subunits along the filament that are need to be simulated at the least. Moreover, the pure state all-atom simulations consist of a periodic filament with 13 identical copies of actin subunit. To generate statistics of equivalent quality, 13 copies of each of the 243 possible combinations of nucleotide states are required to be simulated. To reduce this multi-body complexity to a significant degree, we used a mixing rule to create parameters controlling mixed state interactions from pure state filament parameters. Specifically, in this *mixing* approach, we averaged the intra-subunit interaction parameters (H, σ_h and r_{mh}) from the pure state filaments to obtain parameters for the mixed state. For example, given a CG bead i belonging to an ADPPi bound subunit, and a CG bead j belonging to an ADP bound subunit, the parameter $\sigma_h^{Mix}(i,j)$ between them was obtained as

$$\sigma_h^{Mix}(i,j) = \; 0.5[\sigma_h(\mathrm{ATP}, i,j) + \sigma_h(\mathrm{ADP\text{-}P_i}, i,j)]. \tag{3}$$

To justify our mixing approach, we performed two additional short all-atom simulations of periodic actin filaments made of 26 subunits (with compositions 01001101000001010111110110 and 00010001110111000101100100 respectively, where 0=ADP-P$_\mathrm{i}$, 1=ADP). These two filaments, in presence of the periodic boundary condition, consisted of all $2^5 = 32$ possible combinations of nucleotide states ADP-P$_\mathrm{i}$ and ADP in five consecutive subunits along the filament. An approximate true *average* potential was created by averaging the explicit hENM parameters of each pair (i,j) of CG beads in these filaments (transformed into inverted Gaussian interactions). The discrepancy between the mixing approach and this approximate average potential is summarized in Figure S*2*. We define a mismatch parameter that measures the discrepancy between the force-field parameter σ_h for a pair of CG beads (i,j) derived using the mixing approach

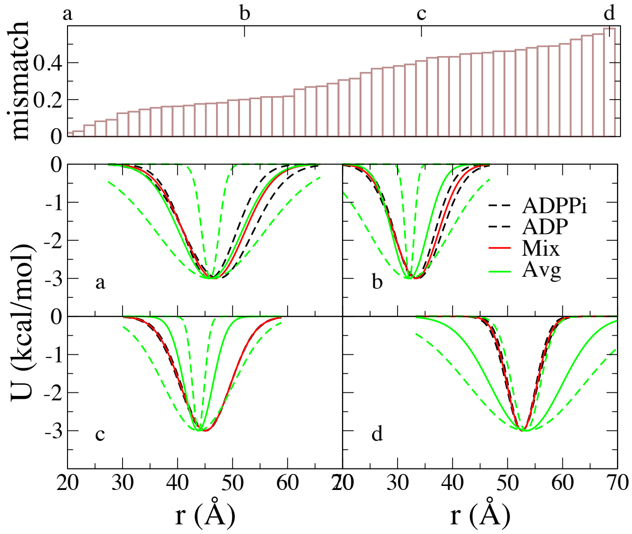

Figure S2: Comparison of the CG pair-wise interaction parameters obtained by using the mixing approach with those in average potential obtained from in the short all-atom simulations. Top panel shows the mismatch parameter, a measure for the difference in pair-wise interaction parameter σ_h obtained by the mixing approach and those in the average potential. The bottom four panels show the interaction potential between four sets of pairs of CG beads belonging to neighboring subunits, corresponding to lowest (panel a), two intermediate (panels b and c) and the largest (panel d) mismatch values (marked with a,b,c and d in the top panel). The interaction potential between a CG bead i belonging to an ADP-P$_i$ bound subunit and a CG bead j, belonging to a ADP bound subunit obtained by using the mixing approach is shown in red, with the corresponding pure state potentials shown as dotted black curves, and the average potential from short all-atom simulations is shown in solid green, with the potentials corresponding to ± 1 standard deviation in parameters H and σ_h shown with the dotted green curves.

($\sigma_h^{Mix}(i,j)$) and that in the average potential obtained from the short all-atom simulations ($\sigma_h^{Avg}(i,j)$).

$$\text{mismatch}(i,j) = \frac{\left|\sigma_h^{\text{Avg}}(i,j) - \sigma_h^{\text{Mix}}(i,j)\right|}{\text{MAX}\left[\sigma_h^{\text{Avg}}(i,j), \sigma_h^{\text{Mix}}(i,j)\right]} \tag{4}$$

Here, σ_h is the inverted Gaussian interaction parameter that characterizes the steepness of the potential energy (Equation (2)). The top panel in Figure S2 shows the mismatch parameter for all pairs of interacting CG beads in our model, plotted with increasing values of the mismatch parameter. Clearly, the mismatch was observed to be small for many pairs of CG beads, but was significant for certain CG bead pairs towards the right-hand side of the plot.

Parameters of the inverted Gaussian interaction for a pair of CG beads in the average potential obtained from the short all-atom simulations varied significantly owing to different combinations of bound nucleotides of the rest of their neighboring subunits along the filament. We calculate the average and standard deviation of the parameters H and σ_h along the filament for each pair of CG beads corresponding to a distinct nucleotide pair. The four panels a, b, c and d on the bottom show the form of the inverted Gaussian potential obtained with the mixing approach and that in the average potential, corresponding to the four pairs of CG beads marked in the top panel (a corresponds to the lowest mismatch, d corresponds to the highest mismatch, and b and c correspond to the intermediate mismatch). It can be seen that even for the pair of CG beads corresponding to the largest mismatch, the potential obtained using the mixing approach was within the variation in the average potential (corresponding ± 1 standard deviation in parameters H and σ_h, shown as dotted green lines in Figure S2) obtained from the all-atom simulations. Given the huge computational advantage balanced by the reasonable accuracy of our rather simple mixing approach, we used it in the rest of this work to obtain interactions between a pair of CG beads corresponding to distinct nucleotide states, acknowledging that alternative choices are possible.

UCG PARAMETER INTERPRETATION

The formulas presented for UCG transitions inherently have a large bearing on the results of the current study. It is therefore useful to note natural assumptions which could produce the rules used. While ideally one would like to know exactly the instantaneous rates as a function of monomer configuration, we do not have access to this data. Instead, we are forced to infer the dependence of a transition probability based on the configuration of the system. We chose to do so by primarily assuming that, for example, the transition state free energy controlling the rate of F-ATP→F-ADP-P_i tracks the pointwise free energy of either the reactants or the products as the configuration of the system changes (i.e. as the reactant free energy changes, the transition state free energy changes similarly). Importantly, if the transition state stability has the same dependence on configuration as the reactants do, then the instantaneous rate of the forward reaction does not change (as it is controlled by the difference in these two energies, and as such will stay constant). Contrastingly, if the stability of the transition state instead follows the products, then the forward reaction will change rate as the protein changes configuration, but the rate of the reverse reactions will stay constant as configuration changes. These concepts are close to the kinetic implications of the Hammond postulate in organic chemistry (24).

Hammond-type dependence has been observed for macroscopic rates and environmental dependence in complex reactions (e.g. protein folding and unfolding (25, 26), and more recently DNA hairpin folding and unfolding (27)). It should be noted that the Metropolis-Hastings criteria was chosen as a convenient approximation which one can interpret via transition states: the cooperativity seen derives from a fluctuating pocket around ATP which moves ATP towards a relatively static barrier. Additionally, the dependence proposed in our study does match the detailed information gained upon flattening actin in our earlier QM/MM studies (28, 29). Unfortunately, no such data is known for phosphate release. The conclusions made in this study primarily focus on the extent of nonlocality observed at the resolution of the MSM and not the fine-grained details of the cooperativity. Clearly, if the individual monomers in the filament did not "feel" the state of a given neighboring monomer, no cooperativity would be observed in the current study. As such, the main conclusions are robust to the exact conformational dependence of the rate imposed.

Whether the transition state stability primarily follows the stability of the reactants or products in the UCG model depends on the parameters of the model and the specific filament configuration considered (additional complexity on the transition state stability is introduced via the dihedral dependence parameters). In the following discussion, we will consider $i \rightarrow j$ the forward reaction. The conditional statement in the Metropolis-Hastings-like rate law switches between the two transition state cases. Specifically, the following conditional

$$\text{MIN}\left[\frac{k_{j\to i}(\phi)}{k_{i\to j}(\phi)}\exp\left[-\beta\left(U_j - U_i\right) - \epsilon_{ij}\right], 1\right]$$

divides our configurational phase space into two sets, with one set satisfying

$$\frac{k_{j\to i}(\phi)}{k_{i\to j}(\phi)}\exp\left[-\beta\left(U_j - U_i\right) - \epsilon_{ij}\right] < 1$$

and the other set defined as its complement. This condition can be rearranged giving

$$-\beta\left(U_j - U_i\right) - \epsilon_{ij} - \log\frac{[0.5 + 0.5\tanh\eta(\phi - \phi_0)]}{[0.5 - 0.5\tanh\eta(\phi - \phi_0)]} < \log\frac{k^0_{i\to j}}{k^0_{j\to i}}$$

Note that when no additional dihedral dependence is added (i.e. $\eta = 0$) the third term on the left side is zero. Roughly, a highly endergonic reaction ($U_j - U_i \gg 0$) forces the transition state to follow the products in stability. More specifically, assuming our rates can be expressed modulo a proportionality constant similarly to the following form from transition state theory, with U denoting free energy and ‡ denoting transition state values

$$\exp\left[-\beta(U^{\ddagger}_{i,j} - U^{corr}_i)\right]$$

we find that we can express the energy of our transition state (modulo a constant) in our first set (that satisfying the given conditional) as

$$U^{\ddagger}_{i,j} = U^{\text{corr}}_j - k_B T \log k_{j\to i}(\phi), \tag{5}$$

where we have assumed that ϵ_{ij} has been incorporated into either U_j or U_i giving corrected energies U^{corr}_j and U^{corr}_i. Importantly, the inverse reaction in the first set shares the same transition state energy; however, as its local energy is given by U^{corr}_j, the rate no longer takes this term into account. While we have only considered the first set in phase space in this paragraph, the second set enjoys the same relations with the role of reactants and products reversed and the appropriate parameters swapped out. The switching point in the transition state behavior is affected by all parameters, but is controlled in practice by setting ϵ_{ij} while other parameters are modified. Additional parameters, e.g. $k^0_{j\to i}$, modify the constant offset in energy and dihedral dependence of the transition state, and η controls the sharpness of the dihedral dependence.

UCG PARAMETER ESTIMATION

There are three parameters in the UCG model for each of the reactions F-ATP $\rightleftharpoons$ F-ADP-P_i and F-ADP-P_i $\rightleftharpoons$ F-ADP + P_i. The prefactor $k^0_{i\to j}$ in absence of the dihedral dependence corresponds to the rate of attempting a subunit from state i to final state j. Here $i, j \in$ [ATP, ADP-Pi, ADP]. The prefactor for the corresponding quantity in the reverse reaction is $k^0_{j\to i}$. The third parameter, Metropolis-Hasting correction factor ϵ_{ij}, was added to account for the lack of a common reference state for the internal energy of the two states.

In the following discussion, $\langle\cdot\rangle$ denotes an average quantity. We need three constraints in order to estimate the three parameters. Two of these constraints are given through matching average values $\langle K_{i\to j}\rangle$ and $\langle K_{j\to i}\rangle$ with known forward and reverse macroscopic rates of reactions $R_{i\to j}$ and $R_{j\to i}$ respectively. The forward macroscopic rate $R_{i\to j}$ of the reaction F-ATP $\rightleftharpoons$ F-ADP-P_i is 0.3 s^{-1} and that for the reaction F-ADP-P_i $\rightleftharpoons$ F-ADP + P_i is 0.0068 s^{-1}. The estimated Gibbs free energy for the reaction F-ATP $\rightleftharpoons$ F-ADP-P_i calculated using metadynamics simulations, ΔG is in the range of -3 to -6 kcal/mol (28, 29). The estimates for the total change in Gibbs free energy for the net reaction F-ATP $\rightleftharpoons$ F-ADP + P_i under physiological conditions varies in a much wider range (30, 31). We chose $\Delta G = -3.2$ kcal/mol for the reaction F-ATP $\rightleftharpoons$ F-ADP-P_i, and $\Delta G = -5.5$ kcal/mol for the reaction F-ADP-P_i $\rightleftharpoons$ F-ADP + P_i. These values of ΔG were used to calculate the reverse reaction macroscopic rates $R_{j\to i}$, using the relationship

$$R_{j\to i} = R_{i\to j}\exp[\beta\Delta G] \tag{6}$$

Due to lack of additional relevant information from the atomistic simulations and from experiments, we imposed the third constraint by specifying the average value of the acceptance probability for the forward reaction sampled in our simulations.

$$\langle p_{i\to j}\rangle \to 0.1 \tag{7}$$

The motivation behind choosing a small average probability of acceptance for the forward reaction was to make the state transitions sensitive towards the potential energy difference between the two states. As $\langle p_{i\to j}\rangle \to 1$, the transitions $i \to j$ become insensitive to the potential energy difference, and the instantaneous transition rate for the forward reaction is simply given by the rate of attempting. The arbitrarily specified value affects the sensitivity of the reaction rates towards the potential energy difference, which in turn depends on the states of neighboring subunits and affects the degree of cooperativity observed in our UCG simulations. Acknowledging this dependence, we used a parameter X later in our kinetic model to vary the extent of the observed cooperativity.

To summarize, the three constraints are

$$\langle K_{i\to j}\rangle = k^0_{i\to j}\left\langle [0.5 + 0.5\tanh\eta(\phi-\phi_0)]\mathrm{MIN}\left[\frac{k_{j\to i}(\phi)}{k_{i\to j}(\phi)}exp\left[-\beta\left(U_j-U_i\right)-\epsilon_{ij}\right],1\right]\right\rangle \to R_{i\to j}$$

$$\langle K_{j\to i}\rangle = k^0_{j\to i}\left\langle [0.5 - 0.5\tanh\eta(\phi-\phi_0)]\mathrm{MIN}\left[\frac{k_{i\to j}(\phi)}{k_{j\to i}(\phi)}exp\left[-\beta\left(U_i-U_j\right)+\epsilon_{ij}\right],1\right]\right\rangle \to R_{j\to i}$$

$$\langle p_{i\to j}\rangle = \left\langle \mathrm{MIN}\left[\frac{k_{j\to i}(\phi)}{k_{i\to j}(\phi)}\exp\left[-\beta\left(U_j-U_i\right)-\epsilon_{ij}\right],1\right]\right\rangle \to 0.1 \tag{8}$$

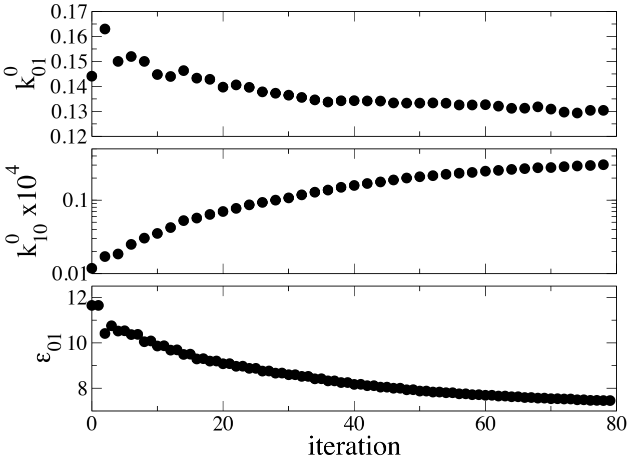

Figure S3: Iterations to obtain the UCG parameters for the reaction F-ATP ⇌ F-ADP-P_i, for $\eta = 0.125$.

Let x_1 be the fraction of the number of times in a simulation run that MIN $\left[\frac{k_{j\to i}(\phi)}{k_{i\to j}(\phi)}\exp[-\beta(U_j - U_i) - \epsilon_{ij}], 1\right] = 1$, and x_2 be the fraction otherwise. The above equations give the following update rules for parameter optimization,

$$\begin{aligned} k^{0,*}_{i\to j} &= k^{0,n}_{i\to j}\frac{R_{i\to j}}{\langle K_{i\to j}\rangle} \\ k^{0,*}_{j\to i} &= k^{0,n}_{j\to i}\frac{R_{j\to i}}{\langle K_{j\to i}\rangle} \end{aligned} \tag{9}$$

$$\epsilon^*_{ij} = \epsilon^n_{ij} + \ln\left[\frac{0.1 - x_1}{x_2\left\langle\left[\frac{k_{j\to i}(\phi)}{k_{i\to j}(\phi)}\, exp[-\beta(U_j - U_i) - \epsilon^n_{ij}]\right]\right\rangle_{\neq 1}}\right] \tag{10}$$

These equations provided a way of performing iterations to optimize the UCG parameters. At iteration n, the following set of update rules was used to obtain a new guess for the parameters.

$$\begin{aligned} k^{0,n+2}_{i\to j} &= \omega k^{0,*}_{i\to j} + (1-\omega)k^{0,n}_{i\to j} \\ k^{0,n+2}_{j\to i} &= \omega k^{0,*}_{j\to i} + (1-\omega)k^{0,n}_{j\to i} \end{aligned} \tag{11}$$

Similarly,

$$\epsilon^{n+1}_{ij} = \omega\epsilon^*_{ij} + (1-\omega)\epsilon^n_{ij} \tag{12}$$

For efficiency, we skipped iterating for $k^0_{i\to j}$ and $k^0_{j\to i}$ in every odd numbered iteration.

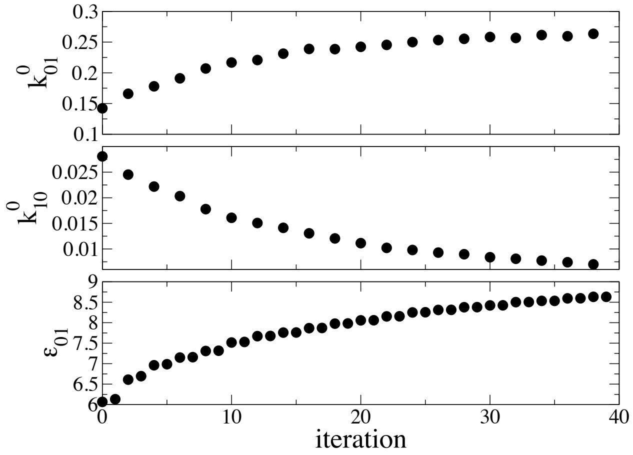

Figure S4: Iterations to obtain UCG parameters for the reaction F-ADP-P$_i$ ⇌ F-ADP + P$_i$, for $\eta = 0$.

ATP hydrolysis

For the reaction F-ATP ⇌ F-ADP-P$_i$, we constructed a long (1040 subunits) F-ATP filament. An initial guess for the UCG parameters was made, making sure that $\langle p_{i\to j}\rangle < 0.1$. For the first iteration $n = 1$, the UCG simulation was run for a sufficiently long time such that all the subunits underwent the forward state transition from ATP (denoted by 0) to ADP-P$_i$ (denoted by 1) at least once, and about $\sim O(10)$ subunits also underwent the reverse state transition. The mean first passage time for the forward and reverse transitions was calculated from these transitions, and was used as an estimate for the inverse of the average transition rates of the corresponding reactions in Equation (4), $\langle K_{i\to j}\rangle^{-1}$ and $\langle K_{j\to i}\rangle^{-1}$ respectively. For faster sampling, a pseudo-UCG simulation was run, such that at each step in the simulation, the term in the denominator of Equation (10) was evaluated for the state transition. However, instead of changing the state of the subunit to ADP-P$_i$ like in regular UCG simulations, it was kept unchanged in the pseudo-UCG simulations.

For efficient sampling of both forward and reverse transition events, we carefully scaled our target macroscopic rates as follows. We used a common scaling factor of 50×10^{-5} to convert the forward and reverse rates from s^{-1} to step^{-1}. Thus, the target forward macroscopic rate was $R_{i\to j} = 1.5\times10^{-4}$ transitions per step, while the target reverse macroscopic rate was $R_{j\to i} = 8.8\times10^{-7}$ transitions per step (Figure S3).

P$_i$ release

A similar procedure was followed to obtain UCG parameters for the P$_i$ release reaction. A common scaling factor of 50×10^{-3} was used to convert the forward and reverse rates from s^{-1} to step^{-1} in our simulations, for efficient sampling of both forward and reverse transition events. The resulting target values were $R_{i\to j} = 3.4\times10^{-4}$ transitions per step for the forward macroscopic rate and $R_{j\to i} = 4.5\times10^{-8}$ transitions per step for the reverse macroscopic rate (Figure S4).

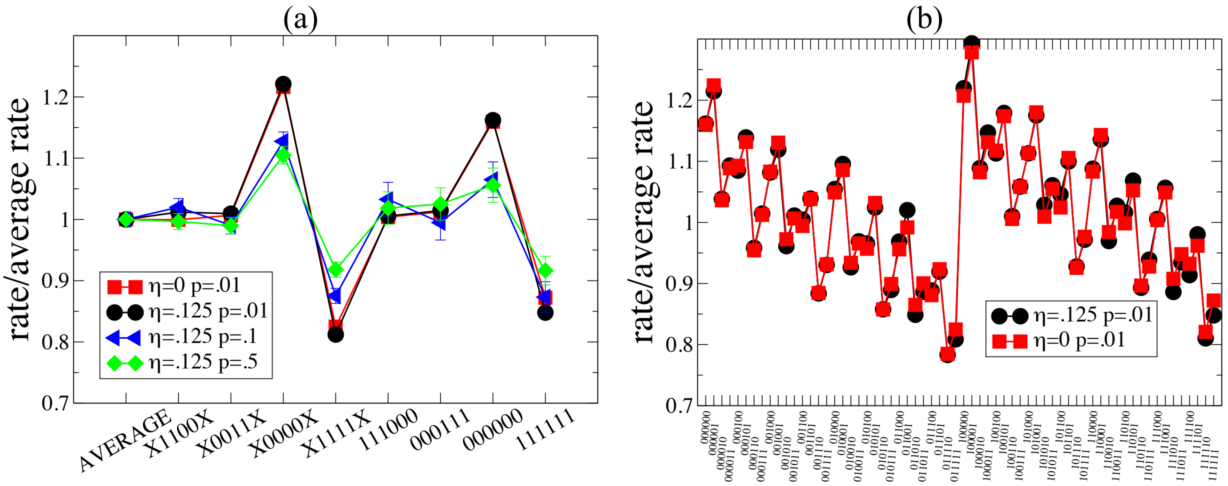

Figure S5: Multi-body effect in ATP hydrolysis, plotted as a ratio of the conditional rate with the average rate. Combinations of neighboring monomer states are indicated using a key on the x-axis, that denotes the state (0=unhydrolyzed, 1=hydrolyzed, X=either) of each of the neighboring subunits, starting from the third neighbor in the pointed-end direction to the third neighbor in the barbed-end direction. (a) Specific combinations of neighbors and (b) all 64 possible combinations of neighbors. Different colors and symbols correspond to different choices of the dihedral angle dependence parameter η and average acceptance probability p, as indicated in the legend. The multi-body effect in ATP hydrolysis is symmetric with respect to the two ends of the filament. Thus, for example, the enhancement in rate for 111000 is approximately equal to that for 000111.

PARAMETER CHOICE AND COOPERATIVITY

In the following section, we demonstrate the effect of choices we made for remaining parameters on the cooperativity observed.

ATP hydrolysis

Figure S5 shows the variation in the multi-body cooperative effect predicted by the UCG model for the ATP hydrolysis reaction, as a function of (a) the presence or absence of the explicit dihedral angle dependence, modulated using η, and (b) the target value of $\langle p_{i\to j}\rangle$ used for UCG parameter estimation. While the former does not significantly affect the predicted cooperativity, the latter was expected to serve as a handle to control the extent of cooperativity. As expected from the form of Equation (8), decreasing $\langle p_{i\to j}\rangle$ increased the model's sensitivity towards multi-body effects.

Figure S6 shows similar variation in the multi-body cooperative effect predicted by the UCG model for the $\mathrm{P_i}$ release reaction, as a function of the value of $\langle p_{i\to j}\rangle$ used for UCG parameter estimation. Figure S7 shows the $\mathrm{P_i}$ release rate variation for all the combinations of neighboring states studied.

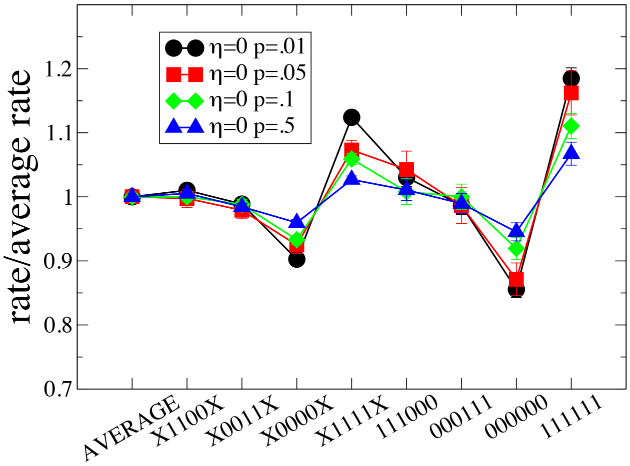

Figure S6: Multi-body effect in P_i release plotted as a ratio of the conditional rate to the average rate. The key on the x-axis is similar to that described in Figure S5 (except for the new definitions 0=ADP-P_i, 1=ADP). Different colors and symbols indicate different values of the average acceptance probability *p* as indicated in the legend.

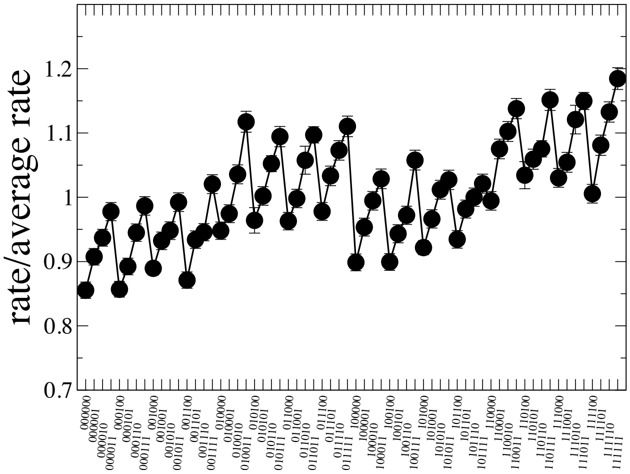

Figure S7: Multi-body effect in P_i release plotted as a ratio of the conditional rate to the average rate for all 64 possible combination of nucleotide states of neighboring subunits. The key on the x-axis is similar to that described in Figure S5. Error bars indicate the standard error for each data-point. The multi-body effect in P_i release is symmetric with respect to the two ends of the filament.

MARKOV STATE MODEL

The kinetic model used in this work is similar to that commonly used in the literature (32, 33), and consisted of the following elementary reactions.

1. Polymerization at the barbed end
2. De-polymerization at the barbed end
3. De-polymerization at the pointed end (only in the conserved system)
4. ATP hydrolysis
5. P_i release

We assumed that transitions associated with (de-)polymerization reactions at the barbed end, de-polymerization reactions at the pointed end, and internal reaction events at each monomer were independent when considering single transitions through the MSM state space. The rates of these transitions, however, each depended on the state vector itself. Let $K_{\text{pol.}}$ denote the polymerization rate, $K_{\text{dis.,barbed}}$ denote the de-polymerization rate at the barbed end, while $K_{\text{dis.,pointed}}$ denote that at the pointed end. Also let $K_{\text{hyd.}}$ and $K_{\text{rel.}}$ denote rates of ATP hydrolysis and P_i release respectively. $K_{\text{dis.,barbed}}$ and $K_{\text{dis.,pointed}}$ are dependent on the state of the terminal subunit at the barbed end and the pointed end respectively. Using the values of these reaction rates provided in Table 1 of the manuscript, the system evolved using a Monte Carlo algorithm with a constant time-step.

The initial condition was chosen such that there are $n_0$subunits present in the filament. The corresponding sequence of states of the nucleotides was stored in a state vector $s[n_0]$ of size n_0. The initial free actin monomer concentration was chosen to be c_0. Let n deote the length of the filament and c denote the free actin monomer concentration at time t. The time-step was chosen as dt and the system is updated at time $t + dt$ based on its state at time t, as follows:

1. A random number uniformly distributed between the interval [0,1] was generated for the barbed-end of the filament.
    a. If the random number was between 0 and $dt{\times}c{\times}K_{\text{pol.,}}$ the polymerization reaction was selected. The length of the filament was updated to $n + 1$ The vector $s[n]$ was expanded to $s[n + 1]$, with the new sequence of states of the nucleotide stored in it.
    b. If the random number was between $dt{\times}c{\times}K_{\text{pol.}}$ and $dt{\times}c{\times}K_{\text{pol.}} + dt{\times} K_{\text{dis.,barbed}}$, then the de-polymerization reaction was chosen. The length of the filament was changed to $n - 1$ The vector $s[n]$ was reduced to $s[n - 1]$, with the new sequence of states of the nucleotide stored in it.
2. A uniform random number was generated for the pointed-end of the filament.
    a. If the random number was between 0 and $dt{\times}K_{\text{dis.,pointed}}$, then the de-polymerization reaction at the pointed end was chosen. The length of the filament was changed to $n - 1$. The vector $s[n]$ was reduced to $s[n - 1]$, with the new sequence of states of the nucleotide stored in it.
3. A set of $n - 2$ uniform random numbers was generated, one for each of the interior subunits in the filament. For each subunit m, the entry $s[m]$ was updated if the random number was between 0 and $dt{\times}K_{\text{react}}$, where $K_{\text{react}} = K_{\text{hyd.}}$ if the state of the subunit was ATP, and $K_{\text{react}} = K_{\text{rel.}}$ if the state of the subunit was ADP-P_i.

In the above, the rates $K_{\text{hyd.}}$ and $K_{\text{rel.}}$ were modulated according to state of neighboring monomers, depending on the degree of cooperativity considered. The cooperativity was not considered for the two terminal monomers (excluding the filament ends) on each side of the filament. In other words, these monomers reacted with the average rates of ATP hydrolysis and P_i release. In the conserved system, the value of c was updated after each de-polymerization reaction took place.

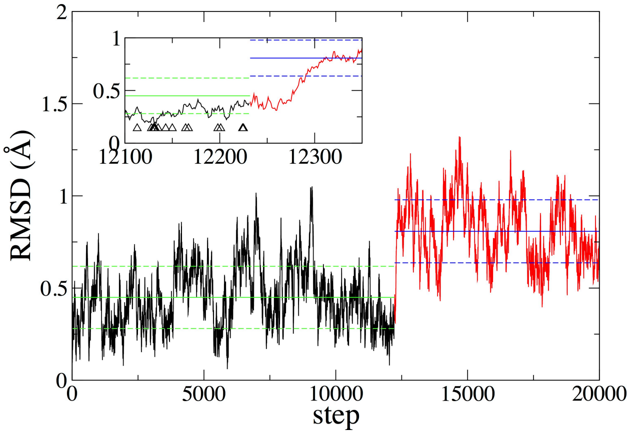

Figure S8: A transition event corresponding to phosphate release in a single subunit from a short simulation run. The simulation setup is similar to that used in obtaining Figure 4 and Figure S7. The root-mean square displacement (RMSD) in positions of CG beads 1-4 of subunit 100 in the filament is shown as a function of simulation steps. The transition corresponding to phosphate release in subunit 100 takes place at step 12232. The RMSD before (black curve) and after (red curve) the transition are shown. The average RMSD before (green line) and after (blue line) the transition are also shown for clarity, along with the range of their variation (± 1 standard deviation, shown as dotted lines with corresponding colors). Inset shows the same data, highlighting the details near the transition event. Steps corresponding to unsuccessful transition attempts by subunit 100 are also shown (inset: black triangles). The subunit configuration reaches a new equilibrium at a faster rate compared to the rates of transition.

The value of dt was carefully chosen to be small enough such that all of the values ($dt \times c \times K_{\text{pol.}} + dt \times K_{\text{dis.,barbed}}$, $dt \times K_{\text{dis.,pointed}}$ and $dt \times K_{\text{react}}$ were significantly less than one at all times. Further modifications were made to the above model depending on the system being simulated, as explained in the manuscript.

MARKOV STATE MODEL DISCRETIZATION AND INTERPRETATION OF KINETICS

Many modern empirically parameterized Markov State Models use state space discretizations which are much finer than the model presented here (34, 35). Systematic analysis of said models has often focused on the quality of this discretization, i.e. the quality and accuracy of the MSM created with respect to the system it approximates. An intuitive metric for a high quality MSM is that the system loses memory when present in a single discrete state: transitions out of a discrete MSM state should not depend on the manner in which one entered said state. It can be seen that the CG configurational dynamics do decouple from the rate of large scale transitions relevant to the MSM derived (Figure S8). This decoupling also legitimizes the use of highly nonequilibrium trajectories for parametrization, as the system is effectively always in conditional equilibrium (36).

The model produced in this work solely aims to capture relaxation timescales which are characterized by the progression of hydrolysis, phosphate release, and (de-)polymerization, which are on the order of seconds or minutes. It is natural to ask how a model which takes into account molecular motions, even at a relatively coarse-grained level, can be propagated using molecular dynamics to see such kinetics. Specifically, we have assumed that the true behavior of the atomistic fluctuations in an actin filament orthogonal to the slow timescale events described in the previous

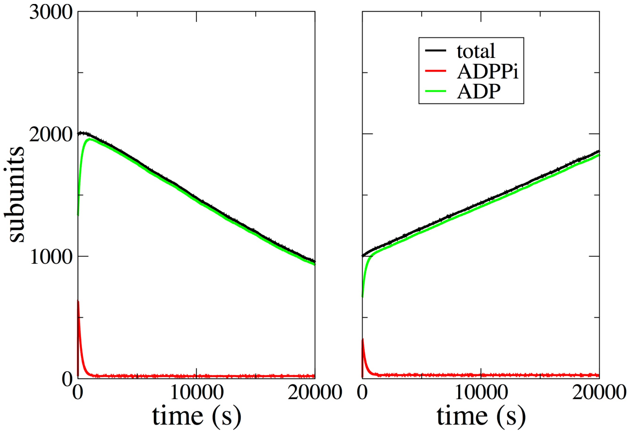

Figure S9: Average number of total subunits and subunits bound to nucleotides ADP-P$_i$ and ADP in the filament as a function of time, for $X = 0$ (left panel, $c = 0.116$ μM) and above (right panel, $c = 0.120$ μM).

paragraph are effectively decoupled: The true biological polymer is assumed to achieve an equilibrium state conditional on the progress of these reactions. As result, the underlying *detailed* dynamics of the system conditional on these reactions is relatively unimportant: the system obeys laws similar to those underpinning transition state theory. Critically, while the CG conformational dynamics are likely dynamically inaccurate with respect to the discrete transitions simulated, they are still decoupled in their relaxation times. As a result, assuming the CG model is parameterized to reproduce equilibrium properties, we argue that configurational dependence on the observed hydrolysis rates are still valid.

FILAMENT DYNAMICS AT CONSTANT FREE ACTIN CONCENTRATION

Figure S9 shows the average contents (ADP-P$_i$ bound and ADP bound subunits) of the filaments, obtained from 1000 statistical runs, as implied by the random hydrolysis mechanism. The initial filament consists of 2/3rd fraction of the filament near the pointed end being ADP bound and the reminder tip near the barbed end made of ATP bound subunits. After a quick initial transient from the chosen initial condition, a steady growth rate with a constant slope for the filament contents is obtained.

SUPPORTING REFERENCES

1. Van der Spoel, D., E. Lindahl, B. Hess, G. Groenhof, A. E. Mark, and H. J. C. Berendsen. 2005. GROMACS: Fast, flexible, and free. *J. Comput. Chem.* 26:1701-1718.
2. Saunders, Marissa G., and Gregory A. Voth. 2012. Comparison between actin filament models: Coarse-graining reveals essential differences. *Structure* 20:641–653.
3. Oda, T., M. Iwasa, T. Aihara, Y. Maeda, and A. Narita. 2009. The nature of the globular- to fibrous-actin transition. *Nature* 457:441-445.

4. Pfaendtner, J., D. Branduardi, M. Parrinello, T. D. Pollard, and G. A. Voth. 2009. Nucleotide-dependent conformational states of actin. *Proc. Natl. Acad. Sci. U.S.A.* 106:12723-12728.
5. Humphrey, W., A. Dalke, and K. Schulten. 1996. VMD: Visual molecular dynamics. *J. Mol. Graph. Model.* 14:33-38.
6. Phillips, J. C., R. Braun, W. Wang, J. Gumbart, E. Tajkhorshid, E. Villa, C. Chipot, R. D. Skeel, L. Kale, and K. Schulten. 2005. Scalable molecular dynamics with NAMD. *J. Comput. Chem.* 26:1781-1802.
7. Bussi, G., D. Donadio, and M. Parrinello. 2007. Canonical sampling through velocity rescaling. *J. Chem. Phys.* 126:014101.
8. Mackerell, A. D., M. Feig, and C. L. Brooks. 2004. Extending the treatment of backbone energetics in protein force fields: Limitations of gas-phase quantum mechanics in reproducing protein conformational distributions in molecular dynamics simulations. *J. Comput. Chem.* 25:1400-1415.
9. Plimpton, S. 1995. Fast parallel algorithms for short-range molecular-dynamics. *J. Comput. Phys.* 117:1-19.
10. Isambert, H., P. Venier, A. C. Maggs, A. Fattoum, R. Kassab, D. Pantaloni, and M. F. Carlier. 1995. Flexibility of actin-filaments derived from thermal fluctuations - effect of bound nucleotide, phalloidin, and muscle regulatory proteins. *J. Biol. Chem.* 270:11437-11444.
11. Chu, J. W., and G. A. Voth. 2006. Coarse-grained modeling of the actin filament derived from atomistic-scale simulations. *Biophys. J.* 90:1572-1582.
12. McCullough, B. R., L. Blanchoin, J. L. Martiel, and E. M. De La Cruz. 2008. Cofilin increases the bending flexibility of actin filaments: Implications for severing and cell mechanics. *J. Mol. Biol.* 381:550-558.
13. Pfaendtner, J., E. Lyman, T. D. Pollard, and G. A. Voth. 2010. Structure and dynamics of the actin filament. *J. Mol. Biol.* 396:252-263.
14. Fan, J., Marissa G. Saunders, and Gregory A. Voth. 2012. Coarse-graining provides insights on the essential nature of heterogeneity in actin filaments. *Biophys. J.* 103:1334–1342.
15. Schramm, A. C., G. M. Hocky, G. A. Voth, L. Blanchoin, J. L. Martiel, and E. M. De La Cruz. 2017. Actin filament strain promotes severing and cofilin dissociation. *Biophys. J.* 112:2624-2633.
16. De La Cruz, E. M., and M. L. Gardel. 2015. Actin mechanics and fragmentation. *J. Biol. Chem.* 290:17137-17144.
17. De la Cruz, E. M., J. L. Martiel, and L. Blanchoin. 2015. Mechanical heterogeneity favors fragmentation of strained actin filaments. *Biophys. J.* 108:2270-2281.
18. De La Cruz, E. M., J. Roland, B. R. McCullough, L. Blanchoin, and J. L. Martiel. 2010. Origin of twist-bend coupling in actin filaments. *Biophys. J.* 99:1852-1860.
19. Otterbein, L. R., P. Graceffa, and R. Dominguez. 2001. The crystal structure of uncomplexed actin in the ADP state. *Science* 293:708-711.
20. Graceffa, P., and R. Dominguez. 2003. Crystal structure of monomeric actin in the ATP state - structural basis of nucleotide-dependent actin dynamics. *J. Biol. Chem.* 278:34172-34180.
21. Chu, J. W., and G. A. Voth. 2005. Allostery of actin filaments: Molecular dynamics simulations and coarse-grained analysis. *Proc. Natl. Acad. Sci. U.S.A.* 102:13111-13116.

22. Fan, J., M. G. Saunders, E. J. Haddadian, K. F. Freed, E. M. De La Cruz, and G. A. Voth. 2013. Molecular origins of cofilin-linked changes in actin filament mechanics. *J. Mol. Biol.* 425:1225-1240.
23. Kang, H., M. J. Bradley, W. A. Elam, and E. M. De La Cruz. 2013. Regulation of actin by ion-linked equilibria. *Biophys. J.* 105:2621-2628.
24. Hammond, G. S. 1955. A correlation of reaction rates. *J. Am. Chem. Soc.* 77:334-338.
25. Dinner, A. R., and M. Karplus. 1999. Is protein unfolding the reverse of protein folding? A lattice simulation analysis. *J. Mol. Biol.* 292:403-419.
26. Alemany, A., B. Rey-Serra, S. Frutos, C. Cecconi, and F. Ritort. 2016. Mechanical folding and unfolding of protein barnase at the single-molecule level. *Biophys. J.* 110:63-74.
27. Alemany, A., and F. Ritort. 2017. Force-dependent folding and unfolding kinetics in DNA hairpins reveals transition-state displacements along a single pathway. *J. Phys. Chem. Lett.* 8:895-900.
28. McCullagh, M., M. G. Saunders, and G. A. Voth. 2014. Unraveling the mystery of ATP hydrolysis in actin filaments. *J. Am. Chem. Soc.* 136:13053-13058.
29. Sun, R., O. Sode, J. F. Dama, and G. A. Voth. 2017. Simulating protein mediated hydrolysis of ATP and other nucleoside triphosphates by combining QM/MM molecular dynamics with advances in metadynamics. *J. Chem. Theory Comput.* 13:2332-2341.
30. Tran, Q. H., and G. Unden. 1998. Changes in the proton potential and the cellular energetics of escherichia coli during growth by aerobic and anaerobic respiration or by fermentation. *Eur. J. Biochem.* 251:538-543.
31. Wackerhage, H., U. Hoffmann, D. Essfeld, D. Leyk, K. Mueller, and J. Zange. 1998. Recovery of free ADP, P-i, and free energy of ATP hydrolysis in human skeletal muscle. *J. Appl. Physiol.* 85:2140-2145.
32. Ranjith, P., K. Mallick, J.-f. Joanny, and D. Lacoste. 2010. Role of ATP-hydrolysis in the dynamics of a single actin filament. *Biophys. J.* 98:1418-1427.
33. Vavylonis, D., Q. Yang, and B. O'Shaughnessy. 2005. Actin polymerization kinetics, cap structure, and fluctuations. *Proc. Natl. Acad. Sci. U.S.A.* 102:8543-8548.
34. Prinz, J. H., H. Wu, M. Sarich, B. Keller, M. Senne, M. Held, J. D. Chodera, C. Schutte, and F. Noe. 2011. Markov models of molecular kinetics: Generation and validation. *J. Chem. Phys.* 134:174105.
35. Bowman, G. R., V. Pande, and F. Noe. 2014. An introduction to Markov state models and their application to long timescale molecular simulation. Springer, Dordrecht.
36. Nuske, F., H. Wu, J. H. Prinz, C. Wehmeyer, C. Clementi, and F. Noe. 2017. Markov state models from short non-equilibrium simulations-analysis and correction of estimation bias. *J. Chem. Phys.* 146:094104.